# Single-Photon CMOS Detectors for HWO

**Edwin Alexani, Justin P. Gallagher, and Donald F. Figer**
*Rochester Institute of Technology, Center for Detectors, Rochester, New York, USA*

The *Habitable Worlds Observatory* (HWO) is NASA's current New Great Observatory concept. HWO will observe the universe with unprecedented instrument stability and detector performance to search for life elsewhere. Currently, no single detector technology can meet HWO's diverse and demanding specifications. However, complementary metal-oxide-semiconductor (CMOS) single-photon counting detectors (SPCDs) already meet some of HWO's Technology Readiness Level (TRL) 5 specifications and are excellent candidates for further development. This paper provides an overview of CMOS SPCDs and characterization results by the Center for Detectors (CfD) at RIT.

## 1. Introduction

The *Habitable Worlds Observatory* (HWO) is NASA's response to the 2020 Decadal Survey recommendation to develop a "future large Infrared/Optical/Ultraviolet telescope optimized for observing habitable exoplanets and general astrophysics" (National Academies of Sciences, Engineering, and Medicine 2023). The Survey emphasizes the project's ambitious scale, requiring "a period of mission and technology maturation." The HWO Technology Development Plan specifies that detectors require significant advancement (Bolcar et al. 2025). This paper describes the potential of CMOS SPCDs for HWO.

## 2. Detector Technology Specifications and Candidates

HWO will observe the universe in the ultraviolet (UV), visible (VIS), and infrared (IR), with three instruments in the current design: the Coronagraph ($\sim 400-1800$ nm), the High-Resolution Imager ($\sim 200 - 2500$ nm), and the UV Multi-Object Spectrograph ($\sim 100-1000$ nm) (Feinberg & Mennsesson 2025). Table 1 lists detector specifications for wavelength regimes identified by the *Habitable Worlds Observatory* Technology Roadmap (hereafter HWO Roadmap, Bolcar & Zhao 2024), including dark current (DC), read noise (RN), and quantum efficiency (QE).

Table 1: Detector Performance Specifications

| | DC ( $e^-$/s/px) | RN ( $e^-$/px) | QE |
|---|---|---|---|
| NUV/VIS | $< 0.002$ | $< 2.5$ | $> 50\%$ |
| Visible | $< 0.0001$ | $< 0.1$ | $> 80\%$ |
| NIR | $< 0.001$ | $< 0.1$ | $> 90\%$ |

The HWO Roadmap identifies prospective detector technologies for the categories in Table 1. The NUV/VIS detector candidates are CMOS SPCDs, electron multiplying charge-coupled devices (EMCCDs), skipper CCDs, and microchannel plates (MCPs). The visible range candidates are CMOS SPCDs, EMCCDs, and skipper CCDs. Options in the NIR are H4RGs, linear-mode avalanche photodiodes (LM-APDs), transition edge sensors (TESs), microwave kinetic inductance detectors (MKIDs), and superconducting nanowire single-photon detectors (SNSPDs).

## 3. CMOS Single-Photon Counting Detectors

The HWO Roadmap identifies CMOS SPCDs as candidate detector technology for HWO. They are candidates because of their low DC, low RN, high QE, radiation tolerance, on-chip digitization, and per-pixel readout. CMOS SPCDs have low RN due to the high input-referred conversion gain (CG), which produces a large voltage response for a small electronic charge stored in the low-capacitance floating diffusion sense node (Gallagher et al. 2024a). The photon counting histogram (PCH) in Figure 1 best represents this performance. Each peak location corresponds to a discrete integer electron number, and the spacing between them is the CG. The depth of the valleys between the peaks is a function of read noise, such that deeper valleys correspond to lower read noise and better electron resolution. CMOS SPCDs exist in formats from 1 Mpx to 163 Mpx (Ma et al. 2022), and pixel sizes ranging from $1 - 10\,\mu$m.

The Center for Detectors (CfD) at RIT has been characterizing two CMOS SPCDs. The first is the Quantum Image Sensor (QIS) by Dartmouth College and Gigajot Technology Inc., with results reported in Gallagher et al. (2022), Gallagher et al. (2024a), and Gallagher et al. (2024b), and the second is the Fairchild Imaging HWK4123 detector. For the latter, we have multiple acquisition systems (Figure 2): 1) two commercial Hamamatsu Photonics K.K. ORCA-Quest C15550-20UP camera heads (hereafter QUEST), and 2) a custom acquisition system designed by RIT and housed in a dewar during characterization (hereafter PHOTRON). The QUEST camera is a proven commercial system used to compare and verify results from the PHOTRON system, ensuring that HWK4123 detectors perform consistently across acquisition systems. We report measurements


Janice C. Lee, Jessica Noviello, Stephanie LaMassa, and Marc Postman, eds., 

for the QUEST and PHOTRON systems in Section 4.

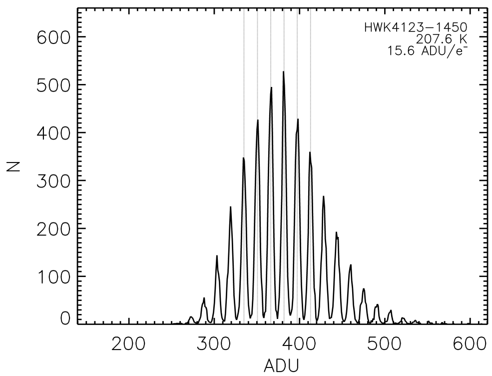


Fig. 1.— The plot shows the PCH for a single HWK4123 pixel, measured with the PHOTRON system. Each peak location is defined by the mean of a Gaussian fit (vertical lines), and is the number of resolved electrons, in ADU. The space between peaks is the CG, here 15.6 ADU/e$^-$.

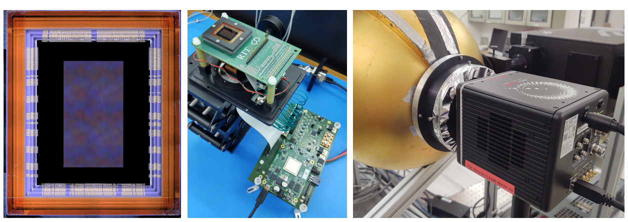

Fig. 2.— *(left)* The image shows the HWK4123 detector. *(center)* The image shows the PHOTRON system outside of the dewar. *(right)* The image shows the QUEST camera mounted on an integrating sphere.

## 4. CMOS SPCD Measurements by CfD

The following sections describe detector characteristics and the measurements made by the CfD for the HWK4123 detector using the QUEST and PHOTRON systems.

### 4.1. Laboratory Measurements

We report measurements of dark current and read noise, quantum efficiency, conversion gain, well depth, and linearity. The results are summarized in Table 2, along with results for the QIS from Gallagher et al. (2024a).

Dark current (DC) is the detector signal in the absence of light, primarily due to thermal electron-hole pair generation. We calculate DC by fitting a line to the signal measured in the dark at different integration times (Figure 3). DC contributes to shot noise and degrades the signal-to-noise ratio (SNR) of faint measurements made by HWO. The DC for the HWK4123 is $\sim 0.022\,e^-$/s/px at 252 K and $\sim 0.00046\,e^-$/s/px at 202 K (Figures 3 and 4). The DC at 202 K meets the HWO DC specification for NUV/VIS ($<0.002\,e^-$/s/px), NIR ($<0.001\,e^-$/s/px), and is $\sim 5$ times larger than the visible range specification (Table 1).

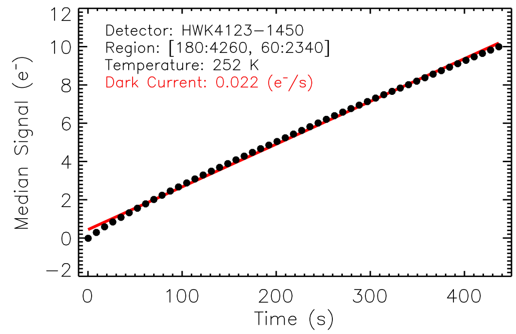


Fig. 3.— The plot shows the signal versus time for the HWK4123 at 252 K, measured with the PHOTRON system. Each dot represents the median signal of the entire detector for 100 frames. The slope of the red line approximates DC.

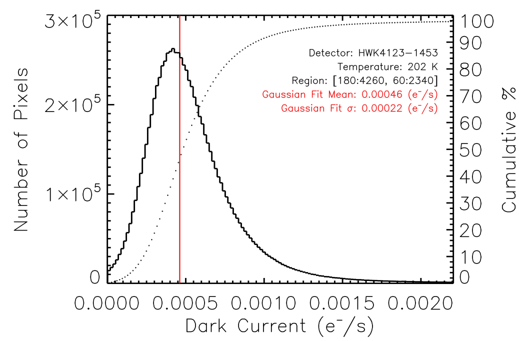


Fig. 4.— The plot shows the histogram of DC per pixel for the HWK4123 at 202 K, measured with the PHOTRON system. The y-axis on the left is the number of pixels per DC bin on the x-axis. The y-axis on the right is the cumulative percentage of pixels up to a DC bin. The vertical red line is the mean of a Gaussian fit to the distribution.

Read noise (RN) is the uncertainty in the measured signal. We measure read noise by calculating the total noise in the signal at the shortest integration time (here 172.8 $\mu$s), such that RN is the dominant source of noise. RN contributes to total noise and degrades the SNR of observations such as exoplanet direct imaging. The RN for the HWK4123 is $0.19\,e^-$/px, measured as the standard deviation in the signal of 10,000 frames. The RN satisfies the HWO UV/VIS RN specification ($<2.5\,e^-$/px).

Quantum efficiency (QE) is the ratio of incident photons to measured photoelectrons. We use a NIST-calibrated diode to determine the number of incident photons and compare to the measured signal. QE affects the amount

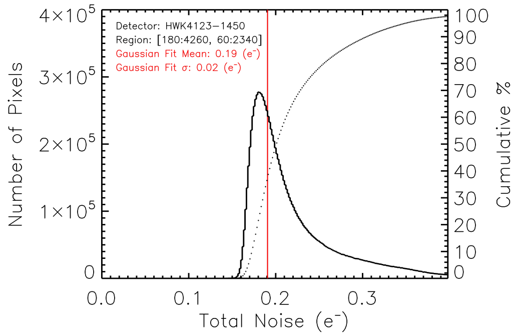


Fig. 5.— The plot shows the total noise histogram for the HWK4123, measured with the PHOTRON system. The y-axis on the left is the number of pixels per total noise bin on the x-axis. The y-axis on the right is the cumulative percentage of pixels up to a total noise bin. The vertical red line is the mean of a Gaussian fit to the distribution.

of time required to reach a desired SNR, which will impact the amount of time HWO needs to observe a target, and affect mission yield. The HWK4123 QE is shown in Figure 6, and peaks at 88% for 485 nm. The QE partially satisfies the HWO specifications in the visible range. At shorter wavelengths, the probability of producing more than one electron increases, which is a phenomenon known as quantum yield (QY). The data are not yet corrected for QY. The CfD is currently measuring QY by following Baggett (2008), although their measurements suggest that QY is only $\sim 1.04 - 1.08$ from $200 - 300$ nm.

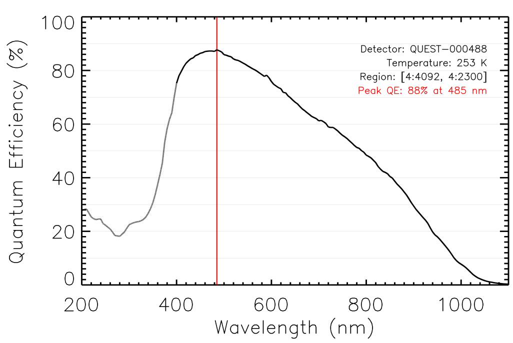


Fig. 6.— The curve shows the HWK4123 QE at 253 K, measured with the QUEST system. The vertical red line shows the peak QE of 88% at 485 nm. The measurements from $200 - 400$ nm are preliminary and marked by dashes.

The photon transfer experiment (PTE) measures signal as a function of fluence. Figure 7 shows the photon transfer curve (PTC) which plots the variance of the signal as a function of fluence. The conversion gain of the detector is the inverse of the slope in the linear portion of the PTC.

The PHOTRON's PTC provides a CG fit of 15.6 ADU/e$^-$ and the detector saturates at $\sim$4,000 ADU for a well depth (WD) of 256 e$^-$ at high gain. The PTE also produces data that we use to measure the linearity of the detector and the WD (Figure 8). Linearity is the fractional countrate (ratio of measured to expected signal) as a function of fluence. The WD is the number of electrons that the storage well (SW) holds at saturation. Astronomical data must be calibrated with the linearity curve, and WD limits the exposure time.

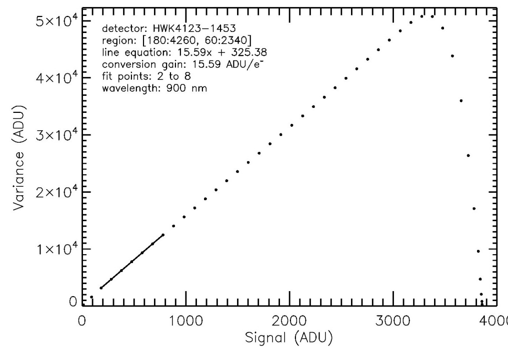


Fig. 7.— The plot shows the PTC of the HWK4123, measured with the PHOTRON system. The y-axis is the variance in signal in ADU, the x-axis is the signal in ADU, and the inverse of the fitted slope is the conversion gain.

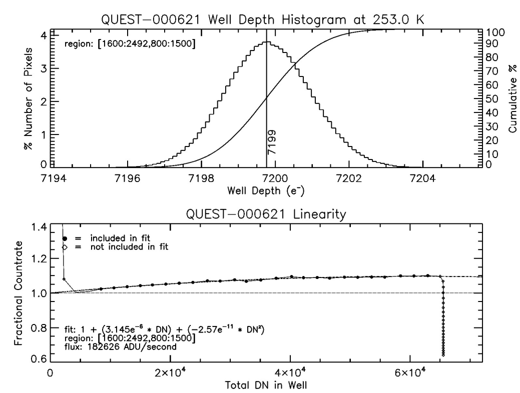


Fig. 8.— Both panels show HWK4123 measurements with the QUEST, which uses a dual-gain mode that provides WD and CG values different from those of a single-gain mode system (such as PHOTRON) (see Hamamatsu Photonics K.K. 2022). *(bottom)* The panel shows the fractional countrate on the y-axis, and fluence on the x-axis. This is the linearity curve, which is fit with a polynomial that is used for calibration. *(top)* The panel shows a histogram of saturated pixels with electron numbers (WD) on the x-axis. The vertical line is the mean of a Gaussian fit to the distribution. The y-axis on the left is the percentage of pixels at a given WD, and the cumulative percentage is on the right.

Persistence is the residual signal in a pixel that was exposed to light and subsequently readout in the dark more than once. Persistence is caused by latent charge due to traps or incomplete clearing during reset. When the signal returns to the known DC value, latent charge is cleared from the pixel. We measured 0.03% of fluence ($1.5\,e^-$) liberated from an after the second read in the dark, and a return to zero by the fourth read. The initial fluence was $5133\,e^-$ and the time between reads was 0.5 s.

Table 2: CMOS SPCD Measurements and Parameters

| | HWK4123 | QIS [a] |
|---|---|---|
| Format [ pixels ] | 4096×2304 | 1024×1024 |
| Pixel Size [ $\mu$m ] | 4.6 | 1.1 |
| DC [ $e^-$/s/px ] | 0.00046 (202 K)<br>0.016 (253 K) [a,*] | 0.0003 (200 K)<br>0.0005 (253 K) [*] |
| RN [ $e^-$/px ] | 0.19 | 0.27 |
| peak QE | 88% (485 nm) | 83% (500 nm) |

[a] Values are from Gallagher et al. (2024a).
[*] Note the pixel area scaling for DC at 253 K.

### 4.2. Astronomical Observations

The CfD evaluates detector performance at ground-based telescopes with astronomical targets to identify performance limitations that may not manifest in the lab. We observed stars in M36 (Figure 9) to evaluate detector characteristics such as linearity and QE. We determine QE in the field by comparing the measured signal for each star to the expected signal based on the catalog reference. We measure linearity in the field by observing stars of different brightness at the same integration time and divide the measured signal by the catalog reference. We also observed extended objects such as NGC7331 (Figure 9). The data are currently being processed.

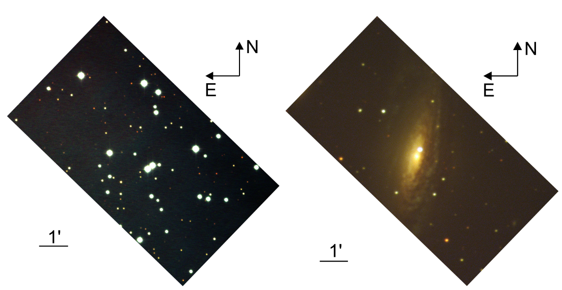


Fig. 9.— *(left)* The image shows the open cluster M36 in the Johnson filters B (blue), V (green), and R (red). *(right)* The image shows the spiral galaxy NGC 7331 in the Johnson filters U (blue), V (green), and I (red), with supernova SN 2025rbs in bluish-white near the galactic core.

## 5. Improving CMOS SPCD QE from 100–1000 nm

The HWO Roadmap specifies the need to improve QE to enable scientific applications. The following sections provide pathways to improve CMOS SPCD QE at shorter ($100-400$ nm) and longer wavelengths ($400-1000$ nm).

### 5.1. Improving QE at Shorter Wavelengths

The HWO requires QE greater than 50% at shorter wavelengths to achieve its science goals. One technique to enhance QE is backside engineering to modify the electric field in the silicon substrate and push charges away from surface traps towards the collection area. Delta-doping is such a technique and uses molecular beam epitaxy to dope the silicon layer with boron (Nikzad et al. 2012). For instance, Hoenk et al. (2009) reported QE from $40-50\%$ in the $100-200$ nm range for a delta-doped CCD detector, and Nikzad et al. (2012) reported QE from $30-60\%$ in the $160-300$ nm range for an anti-reflection-coated delta-doped EMCCD. Further, Hoenk et al. (2022) reported QE from $20-45\%$ in the $200-400$ nm range for a back-illuminated superlattice-doped CMOS detector.

### 5.2. Improving QE at Longer Wavelengths

The HWO requires QE greater than 80% at longer wavelengths to achieve its science goals. One method to improve QE at longer wavelengths is to make thicker pixels to match the absorption length (for silicon based-devices, O'Connor et al. 2006). For instance, Cho & Johnson (2023) compared the QE of the HWK4123 to the HWK1411, which have a pixel thickness of 2.5 $\mu$m and 6.0 $\mu$m respectively. The HWK1411 QE exceeds that of the HWK4123 by approximately ten absolute percentage points from $600-1000$ nm.

## 6. Designing Single-Photon Sensing NIR Detectors

The CfD is prototyping a single-photon sensing NIR photodiode by leveraging the Fossum et al. (2016) SPCD design. We will simulate performance in key metrics like DC, RN, and QE, as a function of materials, doping, bias, temperature, and geometry. The current prototype is shown in Figure 10. The locations of the storage well (SW), the transfer gate (TG) and the floating diffusion (FD) follow the work of Fossum et al. (2016) and Kovacs (2021). If successful, the prototype will provide a NIR detector option for HWO.

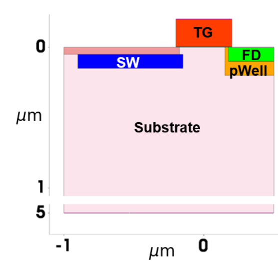


Fig. 10.— The schematic shows a cross-section for a prototype single-photon counting NIR pixel. The y-axis is truncated for display purposes.

## 7. Using Arrayed Waveguide Gratings on HWO

A major goal for HWO is to detect exoplanet biosignatures with a spectrograph. The HWO Technology Development Plan identifies photonics as "enhancing" technology (Bolcar et al. 2025). Arrayed waveguide gratings (AWGs) are compact, on-chip, photonic spectrographs. Combining AWGs with CMOS SPCDs can significantly reduce the size, weight, and power of instruments compared to bulk optic spectrographs such as NIRSpec on JWST. Figure 11 shows the instrument model, and Alexani et al. (2024) simulated observing exoplanets with this technology on HWO.

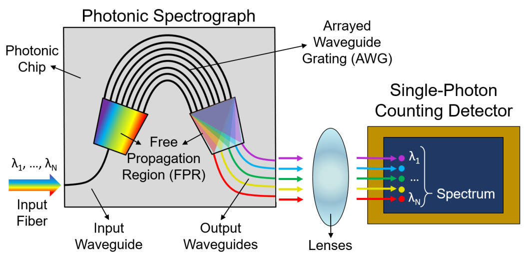


Fig. 11.— The image shows a diagram for a single-photon counting photonic spectrograph. Light enters the photonic chip (shown in gray) through the input fiber. Light disperses in the AWG, and recombines with interference in the output FPR to produce the spectrum which the lenses focus on the detector (Alexani et al. 2024).

## 8. Conclusion

The *Habitable Worlds Observatory* will need improved detector technology to achieve its science goals. CMOS single-photon counting detectors satisfy some of the detector specifications for read noise, dark current, and quantum efficiency. CMOS SPCDs also have reliable and proven technology development pathways, making them promising for HWO.

**Acknowledgments.** The authors acknowledge the University of Rochester for providing access to the C.E.K. Mees Observatory. The authors acknowledge Mason Wolcott for contributions to Figure 10.

## REFERENCES

Alexani, E., Figer, D. F., & Gatkine, P. 2024, in Space Telescopes and Instrumentation 2024: Optical, Infrared, and Millimeter Wave, Vol. 13092, International Society for Optics and Photonics (SPIE), 130925T

Baggett, S. 2008, WFC3 TV3 Testing: Quantum Yield in the UV, WFC3 Instrument Science Report 2008-47, 5 pages. https://ui.adsabs.harvard.edu/abs/2008wfc..rept...47B

Bolcar, M. R., & Zhao, F. 2024, Exoplanet Exploration Program Office Webinar Series, 31. https://exoplanets.nasa.gov/internal_resources/3152/HWO%20technology%20roadmap%20presentation.pdf

Bolcar, M. R., Zhao, F., Scowen, P., et al. 2025, HWO25 – Towards the Habitable Worlds Observatory: Visionary Science and Transformative Technology, 25. https://ntrs.nasa.gov/api/citations/20250007159/downloads/Bolcar_HWOTechRoadmaps_HWO25_20250729_v3.pdf?attachment=true

Cho, K. B., & Johnson, B. 2023, in IISW, International Image Sensor Society

Feinberg, L. D., & Mennsesson, B. 2025, HWO Face to Face Meeting, 23. https://ntrs.nasa.gov/api/citations/20240006492/downloads/Exploratory%20and%20Analytic%20Cases%20HWO.pdf

Fossum, E. R., Ma, J., & Masoodian, S. 2016, in Advanced Photon Counting Techniques X, Vol. 9858, International Society for Optics and Photonics (SPIE), 985805

Gallagher, J. P., Buntic, L., Alexani, E., et al. 2024a, in X-Ray, Optical, and Infrared Detectors for Astronomy XI, Vol. 13103, International Society for Optics and Photonics (SPIE), 131030S

Gallagher, J. P., Buntic, L., Deng, W., et al. 2024b, Journal of Astronomical Telescopes, Instruments, and Systems, 10, 036003

Gallagher, J. P., Buntic, L., Figer, D. F., et al. 2022, in X-Ray, Optical, and Infrared Detectors for Astronomy X, Vol. 12191, International Society for Optics and Photonics (SPIE), 121910T

Hamamatsu Photonics K.K. 2022, ORCA-Quest qCMOS camera C15550-20UP Technical note. https://camera.hamamatsu.com/content/dam/hamamatsu-photonics/sites/documents/99_SALES_LIBRARY/sys/SCAS0154E_C15550-20UP_tec.pdf

Hoenk, M. E., Jones, T. J., Dickie, M. R., et al. 2009, in Infrared Systems and Photoelectronic Technology IV, Vol. 7419, International Society for Optics and Photonics (SPIE), 74190T

Hoenk, M. E., Jewell, A. D., Kyne, G., et al. 2022, in X-Ray, Optical, and Infrared Detectors for Astronomy X, Vol. 12191, International Society for Optics and Photonics (SPIE), 1219113

Kovacs, R. G. 2021, Master's thesis, Rochester Institute of Technology. https://ridl.cfd.rit.edu/products/theses%20and%20senior%20projects/Reid%20Kovacs%20MS%20GradPaper.pdf

Ma, J., Chan, S., & Fossum, E. R. 2022, IEEE Transactions on Electron Devices, 69, 2824

National Academies of Sciences, Engineering, and Medicine. 2023, Pathways to Discovery in Astronomy and Astrophysics for the 2020s (Washington, DC: The National Academies Press)

Nikzad, S., Hoenk, M. E., Greer, F., et al. 2012, Appl. Opt., 51, 365

O'Connor, P., Radeka, V., Figer, D., et al. 2006, in High Energy, Optical, and Infrared Detectors for Astronomy II, Vol. 6276, International Society for Optics and Photonics (SPIE), 62761W